Synthesis and Biological Response of Size-Specific, Monodisperse Drug–Silica Nanoconjugates

Li Tang,[†] Timothy M. Fan,[‡] Luke B. Borst,[§] and Jianjun Cheng[†,*]

[†]Department of Materials Science and Engineering and [‡]Department of Veterinary Clinical Medicine, University of Illinois at Urbana—Champaign, Urbana, Illinois 61801, United States and [§]Department of Population Health and Pathobiology, North Carolina State University, Raleigh, North Carolina 27606, United States

ABSTRACT

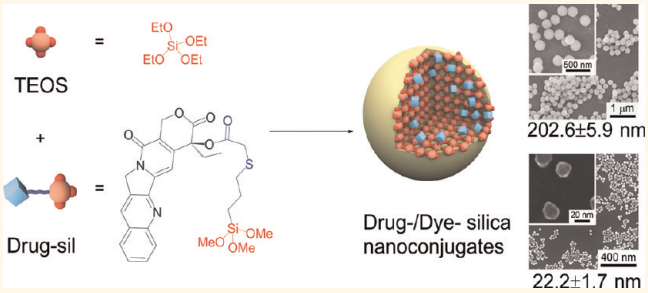

Drug-containing nanoparticles (NPs) with monodisperse, controlled particle sizes are highly desirable for drug delivery. Accumulating evidence suggests that NPs with sizes less than 50 nm demonstrate superior performance *in vitro* and *in vivo*. However, it is difficult to fabricate monodisperse, drug-containing NPs with discrete sizes required for studying and characterizing existing relationships among particle size, biologic processing, and therapeutic functionality. Here, we report a scalable process of fabricating drug–silica conjugated nanoparticles, termed drug–silica nanoconjugates (drug-NCs), which possess monodisperse size distributions and desirable particle sizes as small as 20 nm. We find that 20 nm NCs are superior to their 50 and 200 nm NC analogues by 2–5- and 10–20-fold, respectively, with regard to tumor accumulation and penetration and cellular internalization. These fundamental findings underscore the importance and necessity of further miniaturizing nanomedicine size for optimized drug delivery applications.

KEYWORDS: silica nanoparticle · nanoconjugates · chemotherapeutics · nanomedicine · drug delivery · cancer therapy · tumor penetration · cell uptake · nanoparticle biodistribution

Nanomedicines in the form of polymer–drug conjugates, micelles, nanoparticles (NPs), and vesicles have been extensively studied in the past 2–3 decades for drug and gene delivery applications.[1–9] Although promising, the clinical translation of nanomedicines has proven very difficult.[3] Numerous studies have been designed and performed using nanomedicine as a new modality for improved cancer treatment. However, very few nanomedicines have ever been clinically evaluated and even less have been approved for clinical cancer treatment.[10,11] Although no generalized pathway exists for the clinical translation of nanomedicine, there is a consensus that a clinically applicable nanomedicine should possess controlled physicochemical and pharmacological properties. Specifically, such nanomedicine should have controlled size with low size dispersity, high drug loading, high loading efficiency, controlled drug release kinetics, and sufficient stability and capability of staying nonaggregated in biological media. It should also be easily manufactured at a large scale, from grams up to kilogram scale, and lyophilized to form solid formulation. Very few nanomedicine systems can meet all of these formulation requirements that are critical to their clinical translation.

There has been growing interest in using nanomedicines for targeted or personalized cancer therapy.[1,2] Accumulating evidence shows that the size of nanomedicine plays a vital role in controlling systemic and lymphatic biodistribution, tumor targeting and penetration, and cellular internalization of drug delivery vehicles.[12–23] NPs with size controlled within 20–60 nm have been particularly interesting and actively pursued because some recent studies showed that NPs within this size range have distinct biodistribution, tumor penetration, and cellular trafficking properties that are critical to the *in vivo* use of nanomedicine. For instance, Tseng and his team reported that 30 nm NPs were able to drain into the local auxiliary lymph nodes with high efficiency after footpad administration of NPs while the 100 nm NPs were nearly undetectable in these tissues.[24] Chan and his co-workers reported that 20 and 60 nm gold NPs, as model drug delivery systems, permeated tumor tissues much more rapidly than 100 nm particles *in vivo*.[25] Similar results were also reported by Pun and co-workers.[26] Jing *et al.*

* Address correspondence to jianjunc@illinois.edu.

Received for review January 12, 2012 and accepted April 11, 2012.

Published online April 11, 2012
10.1021/nn300149c

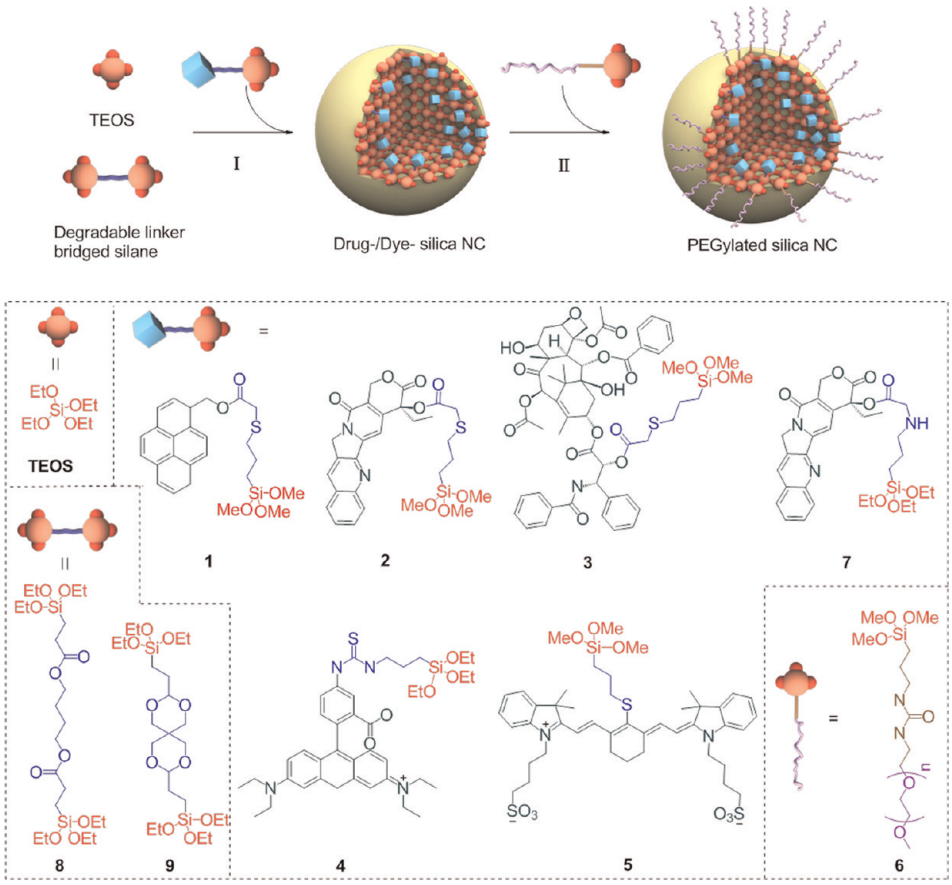

Scheme 1. Drug/dye−silica nanoconjugate. Schematic illustration of the synthesis of drug/dye−silica nanoconjugates (NCs). The Stöber method (St) or the reverse microemulsion method (Trx) (I) was used to prepare drug/dye−silica NCs followed by *in situ* surface PEGylation (II). For NCs formed *via* the St method, TEOS was used in a solution of NH_4OH/MeOH in the presence of 1, 4, or 5 or in a solution of NaF/MeOH in the presence of 2, 3, or 7. For NCs prepared *via* the Trx method, 8 or 9 was used in conjunction with 2 or 3 to synthesize the corresponding NCs.

reported that 40−50 nm NPs outperformed NPs in different size ranges for altering signaling processes that regulate various cellular functions.[15]

Nanomedicines are typically prepared through bottom-up approaches, such as self-assembly of amphiphilic copolymers for the preparation of micelles or vesicles, and nanoprecipitation of hydrophobic polymers for the preparation of NPs. The micellation, vesiclization, and nanoprecipitation methods certainly allow for facile preparation of nanomedicines at a large scale. However, the drawbacks of these formulation methods are also obvious; the resulting micelles, vesicles, or NPs often have broad particle size distributions and variable, sometimes uncontrolled, drug loading and release profiles. It is also extremely difficult to prepare NPs with narrow or monodisperse size that is controlled within 100 nm using these conventional technologies. There are even less reports of the *in vitro* and *in vivo* properties of NPs with discrete size less than 50 nm.[13,15,24,25,27] Here, we report the synthesis of drug−silica conjugated NPs (Scheme 1), termed drug−silica nanoconjugates (drug-NCs) and denoted as drug(dye)X (X = particle size in nm), which can be formulated at nearly any sizes ranging between 20 and 200 nm with monodisperse size distribution (less than 10% coefficient of variation (CV), the ratio of the standard deviation to the mean of particle size), 10−20% drug loading, and controlled drug release profiles. These drug-NCs can be easily prepared on a gram-scale but still with perfectly controlled size and monodisperse size distribution. They showed size-dependent cell uptake, biodistribution, and tumor penetration capability. By addressing several formulation/development issues (*e.g.*, salt stability, scalability, and lyophilizability, *etc.*), we developed a potentially clinically applicable drug(dye) delivery nanomedicine platform that can be precisely controlled and formulated at any size between 20 and 200 nm on a large scale.

RESULTS AND DISCUSSION

Silica NPs can be easily prepared on a large scale with discrete, monodisperse particle sizes through the condensation reaction of tetraethylorthosilicate (TEOS) or tetramethylorthosilicate (TMOS). For example, monodisperse silica spheres with controlled sizes (50 nm−2 μm) can be prepared in a reaction mixture of water, alcoholic solvent, ammonia, and alkyl silicate ester by controlling alcoholic solvents, different alkyl silicate esters,

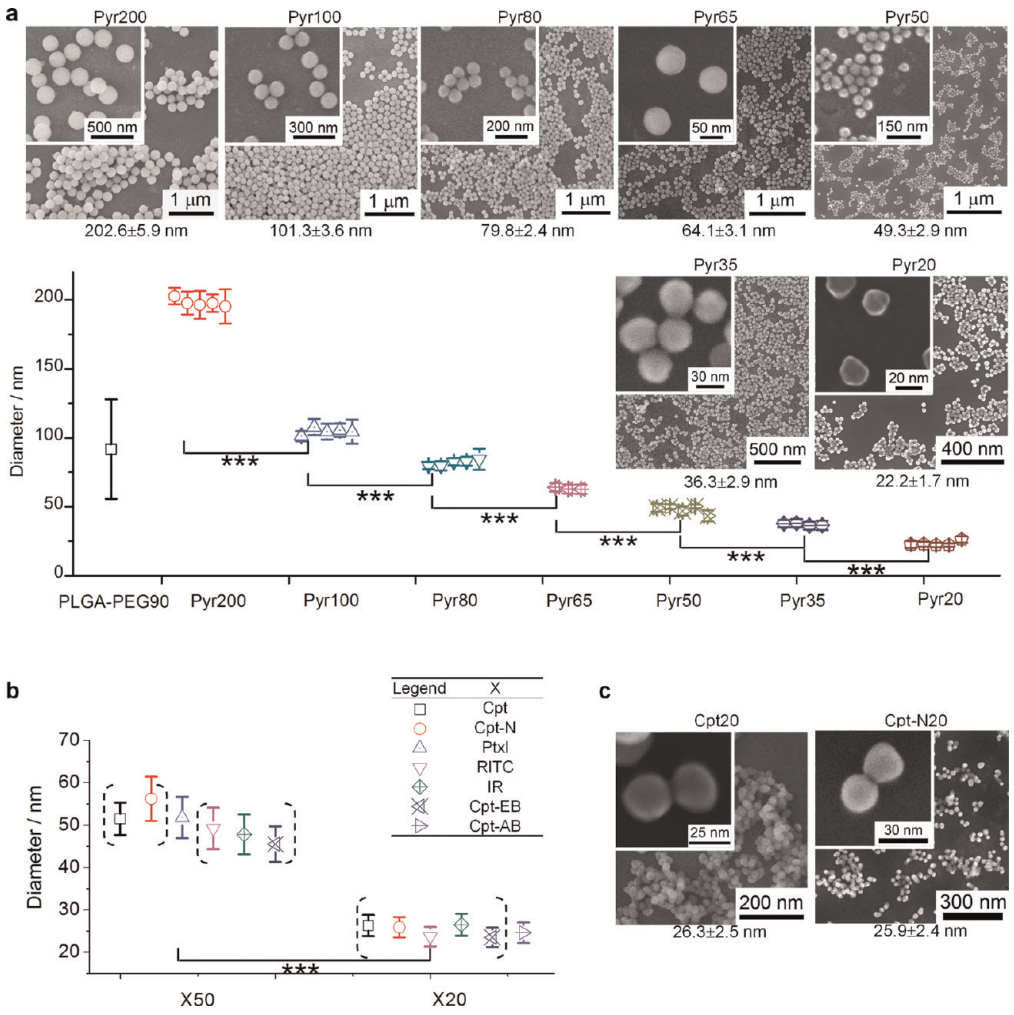

Figure 1. Precise size control of drug/dye−silica nanoconjugates. (a) Preparation of pyrene−silica nanoconjugates (Pyr-NCs) with discrete sizes ranging from 20 to 200 nm. Three to five separate batches of Pyr-NCs for each size were prepared to demonstrate the consistency in size control and batch-to-batch reproducibility. The diameters of NCs were determined by measuring the particle size of 100 particles in representative SEM images (mean ± standard deviation). The difference of NC diameters between each size group is extremely statistically significant with 99.9% confidence (Student's *t* test (two-tailed), ***$p < 0.001$). The SEM images of NCs of each size (20, 35, 50, 65, 80, 100, and 200 nm) were displayed; the higher resolution images of NCs of the corresponding size are shown in the inset. (b) Preparation of different drug/dye−silica NCs with sizes of 50 and 20 nm. (c) SEM images of Cpt20 and Cpt-N20 as the examples to show the excellent size control and monodispersity of NCs with sizes of 20 nm.

as well as the concentration of each component.[28] Silane coupling agents containing a trialkoxysilane group can be readily incorporated into silica NPs during such condensation reaction.[29] We reasoned that trialkoxysilane-containing drugs (dyes) (linked through a degradable ester bond as shown in Scheme 1) should be able to be condensed with TEOS or TMOS to allow the drug (dye) molecules to be incorporated into the resulting silica NPs, which can be released through the cleavage of the ester linker. To demonstrate this concept, we started with **1**, a trimethylorthosilicate that contains pyrenemethanol (Pyr-OH) as a model drug. By controlling the reaction conditions, we were able to prepare Pyr-NCs with discrete sizes 15 nm apart between 20 and 80 nm. As shown in Figure 1a and Table 1 (entries 1−5), NCs with sizes of 22.2 ± 1.7 nm (Pyr20), 36.3 ± 2.9 nm (Pyr35), 49.3 ± 2.9 nm (Pyr50), 64.1 ± 3.1 nm (Pyr65), and 80 nm (Pyr80) can be readily prepared in multigram quantities. To test the reproducibility of these conditions to prepare NCs with the corresponding size, we repeated each experiment 3−5 times and found that the NCs with the desired size could be precisely produced each time. For instance, the five experiments for making Pyr20 under the same condition resulted in particles with sizes of 22.2 ± 1.7, 22.7 ± 2.4, 22.9 ± 1.9, 22.2 ± 1.1, and 26.2 ± 2.4 nm (Figure 1a). The CV values of these five experiments are 7.7, 10.6, 8.3, 5.0, and 9.2%, respectively, with an average CV value of 8.1%. The low CV values (<10%) of Pyr20-NC indicate that these particles are technically monodisperse by industry standard.[30] The conditions of making pyrene-containing NCs of 35, 50, 65, and 80 nm showed similar control over NC size, monodispersity, and reproducibility (Figure 1a). The hydrodynamic sizes of these Pyr-NCs were also measured by dynamic light

TABLE 1. Preparation of Drug/Dye–Silica Nanoconjugates[a]

entry	name of NC	drug/dye	formulation[b]	method[c]	D[d] (nm)	SD[d] (nm)	CV%[e]	IE[f] (%)	LD[g] (wt %)
1	Pyr20	Pyr	TEOS/**1** (29.4/1)	St-A	26.6	2.7	10.2	N/A	N/A
2	Pyr35	Pyr	TEOS/**1** (29.4/1)	St-B	36.3	2.9	8.0	N/A	N/A
3	Pyr50	Pyr	TEOS/**1** (29.4/1)	St-C	43.4	3.9	9.0	N/A	N/A
4	Pyr65	Pyr	TEOS/**1** (29.4/1)	St-D	64.1	3.1	4.8	N/A	N/A
5	Pyr80	Pyr	TEOS/**1** (29.4/1)	St-E	84.4	7.6	9.0	N/A	N/A
6	Pyrl00	Pyr	TEOS/**1** (29.4/1)	St-F	104.4	8.8	8.4	N/A	N/A
7	Pyr200	Pyr	TEOS/**1** (29.4/1)	St-G	195.3	12.8	6.6	N/A	N/A
8	PLGA-PEG90[h]	N/A	PLGA-PEG	NPP	91.8	36.0	39.2	N/A	N/A
9	Cpt20	Cpt	TEOS/**2**/**6** (2.2/1/0.14)	St-A	26.3	2.5	9.5	81.2	24.0
10	Cpt50	Cpt	TEOS/**2**/**6** (2.2/1/0.14)	St-C	51.5	3.8	7.4	82.9	24.0
11	Cpt100	Cpt	TEOS/**2**/**6** (2.5/1/0.14)	St-F	96.1	8.8	9.2	86.5	16.9
12	Cpt200	Cpt	TEOS/**2**/**6** (2.2/1/0.14)	St-G	222.7	16.5	7.4	80.7	24.0
13	Ptxl50	Ptxl	TEOS/**3**/**6** (8.1/1/0.40)	St-C	51.8	4.9	9.5	80.7	13.4
14	RITC20	RITC	TEOS/**4**/**6** (58.8/1/3)	St-A	23.7	2.3	9.7	N/A	N/A
15	RITC50	RITC	TEOS/**4**/**6** (58.8/1/3)	St-C	49.2	4.9	10.0	N/A	N/A
16	RITC200	RITC	TEOS/**4**/**6** (58.8/1/3)	St-G	188.9	14.4	7.6	N/A	N/A
17	IR20	IR	TEOS/**5**/**6** (58.8/1/3)	St-A	26.5	2.6	9.8	N/A	N/A
18	IR50	IR	TEOS/**5**/**6** (58.8/1/3)	St-C	47.8	4.7	9.8	N/A	N/A
19	IR200	IR	TEOS/**5**/**6** (58.8/1/3)	St-G	206.9	16.2	7.8	N/A	N/A
20	Cpt-N20	Cpt	TEOS/7/**6** (3.8/1/0.20)	St-A	25.9	2.4	9.3	79.3	15.9
21	Cpt-N50	Cpt	TEOS/**7**/**6** (3.8/1/0.20)	St-C	56.2	5.2	9.3	83.2	16.6
22	Cpt50*[i]	Cpt	TEOS/**3**/**6** (88.2/1/9.0)	St-C	46.2	4.6	10.0	84.8	1.0
23	Cpt-EB20	Cpt	**8**/**2**/**6**(6.1/1/0.30)	Trx-A	23.5	2.3	9.8	87.5	13.8
24	Cpt-EB50	Cpt	**8**/**2**/**6** (6.0/1/0.30)	Trx-B	45.5	4.2	9.2	93.3	14.6
25	Cpt-AB20	Cpt	TEOS/**9**/**2**/**6** (3.0/3.0/1/0.30)	Trx-C	24.6	2.4	9.8	90.6	14.2
26	Ptxl-EB20	Ptxl	**8**/**3**/**6** (9.0/1/0.40)	Trx-A	22.7	2.2	9.7	77.4	8.8

[a] Formulation of monodisperse, size-specific drug/dye–silica NCs. NCs were denoted as drug(dye)X (X = the size of particles in nm). Abbreviation of drug and dye: Pyr =1-pyrenemethanol, Cpt = camptothecin, Ptxl = paclitaxel, RITC = rhodamine B isothiocyanate, IR = IR783. [b] Substrates used for the silica NC formulation presented in mass ratio. [c] NCs with perfect size control were formulated either using the St-X (X = A–G) conditions (Supporting Information Table S1) or the Trx-X (X = A–C) conditions (Table S2); NPP = nanoprecipitation. [d] NC sizes were characterizes by SEM. Average diameter (D) and standard deviation (SD) were calculated by measuring 100 NCs in a representative SEM image. [e] CV% = SD/D. [f] IE = Incorporation efficiency. [g] LD = Drug loading. [h] Poly(lactide-*co*-glycolide)-*b*-methoxy-PEG ($PLGA_{13k}$-$mPEG_{5k}$) nanoparticle prepared by nanoprecipitation and used as a negative control. [i] Gram-scale preparation of Cpt-NC with 50 nm particle size.

scattering (DLS) (Supporting Information Table S3), which are larger than the hard core sizes measured by scanning electron microscopy (SEM). All of the PDI values measured by DLS are below or around 0.1, indicating again the high monodispersity of these Pyr-NCs. To be consistent, all NC (NP) sizes and size distributions reported in the following part of this paper, except for those in Figure 4b, Table 2, and Table S3, were determined based on the SEM data of the particles, by averaging the particle size of a representative SEM image containing at least 100 particles.

NCs with a particle size of 100 nm or larger should be easier to prepare compared to smaller particles. As expected, both 100 and 200 nm Pyr-NCs (Pyr100 (101.3 ± 3.6 nm) and Pyr200 (202.6 ± 5.9 nm)) were prepared with monodisperse size distribution (CV < 10%) and high reproducibility (Figure 1a and entries 6 and 7 in Table 1). Statistical significances ($p < 0.001$) were found for all NCs with adjacent sizes between 20 and 200 nm. We compared the silica NCs with polymeric NPs prepared through nanoprecipitation (NPP) of amphiphilic copolymers and demonstrated the difference between these two methods for particle size control. Silica NCs can be easily prepared with monodisperse size distributions (CV < 10%). However, polymeric NPs prepared through NPP methods have polydisperse size distribution. For instance, poly(lactide-*co*-glycolide)-*b*-methoxy-PEG (PLGA-PEG) diblock copolymer with a 13 kDa PLGA block and 5 kDa PEG, was precipitated to form PLGA-PEG NPs. The resulting PLGA-PEG NPs showed a much broader size distribution as compared to silica NCs (CV = 39.2%, entry 8, Table 1; Figure S1).

We next attempted to incorporate therapeutics and dyes to silica NCs using the same reactions under similar conditions. Camptothecin (Cpt), a cytotoxic chemotherapeutic agent which inhibits the DNA enzyme topoisomerase I, was converted to the corresponding silane derivative **2** (Scheme 1), with Cpt connected to a trialkoxysilane group *via* a hydrolyzable thioether ester linker, and then incorporated into the silica NCs under similar conditions used for preparing Pyr-NCs with similar sizes. As expected, remarkable control over particle size was observed for the reaction, which resulted in monodisperse Cpt-NCs in all corresponding sizes (entries 9–12, Table 1). For the Cpt-NCs with expected sizes of 20, 50, 100, and 200 nm, the obtained NC sizes were 26.3 ± 2.5, 51.5 ± 3.8, 96.1 ± 8.8, and 222.7 ± 16.5 nm (Figure 1b and Figure S2).

We also attempted to incorporate other therapeutic agents (*e.g.*, paclitaxel (Ptxl)) or fluorescent dyes (*e.g.*, rhodamine B isothiocyanate (RITC) and IR783) using a similar approach with corresponding silane reagents (**3**−**5**) to prepare 20 and 50 nm NCs (Figure 1b). As expected, all obtained NCs containing Ptxl, RITC, or IR783 were monodisperse (CV < 10%) and had the expected particles size (entries 13−19, Table 1). In order to increase the systemic circulation half-life and reduce aggregation of NCs in blood,[31] the surface of NCs was modified with PEG *via* the use of 1-(2-(2-methoxyethoxy)ethyl)-3-(3-(trimethoxysilyl)propyl)urea ($mPEG_{5k}$-sil) **6** (Scheme 1). The resulting PEGylated NCs displayed remarkable stability in both PBS (1×) and cell medium containing 10% fetal bovine serum (FBS) (Figure S3); the NC size remained unchanged for hours.

After we prepared drug(dye)-NCs with precisely controlled sizes, we next studied the size effect of the new drug delivery system on their *in vivo* biodistribution, tumor tissue penetration, and cellular internalization. All silica NCs involved in the following *in vitro* and *in vivo* studies have the identical surface property, spherical shape, and chemical structure and composition in each study with the particle size as the only parameter being changed. PEGylated silica NCs with discrete sizes of 20, 50, and 200 nm containing RITC (termed RITC20, RITC50, and RITC200, respectively) were prepared at a mass ratio of TEOS/**4/6** = 58.8/1/3 (entries 14−16, Table 1, and Figure S4). To facilitate *in vivo*/*ex vivo* analysis of fluorescent NCs with reduced autofluorescence, we prepared PEGylated NCs containing IR783, a near-infrared (NIR) dye at a mass ratio of TEOS/**5/6** = 58.8/1/3; the resulting NIR-active NCs with discrete sizes of 20, 50, and 200 nm were denoted as IR20, IR50, and IR200, respectively (entries 17−19, Table 1 and Figure S5).

In the *in vivo* biodistribution study of IR20, IR50, or IR200 using C57BL/6 mice bearing subcutaneously implanted Lewis lung carcinoma (LLC), tail vein intravenous (i.v.) administration of the NCs followed by tissue harvesting 24 h later showed that a majority of NCs were accumulated in liver and spleen, few were in the respiratory and urinary systems (Figure 2a). The fluorescence of IR783 was found to have excellent tissue transmission; the IR783 concentration can be quantitatively assessed in tissues with a thickness of 2 mm or less (Figure S6). Importantly, NCs with smaller sizes distributed and accumulated in the tumor tissue more efficiently than NCs of larger sizes (Figure 2b). The injected doses of NCs normalized for tumor tissue weight (ID%/g) were 4.18 ± 0.81, 0.98 ± 0.59, and 0.52 ± 0.05 for IR20, IR50, and IR200, respectively. A decrease in particle size by 2.5-fold from 50 to 20 nm resulted in an increase of NC concentration by 330% in tumor tissue (from 0.98 to 4.18, $^{**}p < 0.01$). In comparison, a decrease in particle size by 4-fold from 200 to 50 nm resulted in an increase of NC concentration in tumor tissue by only 88% (from 0.52 to 0.98). NC size showed significant influence on the systemic and tissue biodistribution, and this effect was more profound for NCs below 50 nm in size. These results underscore the importance of studying nanomedicines with sizes less than 50 nm.

As the silica NCs used in our study do not have a targeting ligand, the accumulation of these NCs should follow the enhanced permeation and retention (EPR) effect,[32] a widely recognized passive targeting mechanism, for their accumulation and retention in the tumor tissues. While the NCs extravasate the leaky vasculatures into the tumor tissues, the capability for the NCs to diffuse away from the capillary blood vessels and vasculature should have significant effect on the retention of NCs. We went on and studied the dependence of size on diffusion and penetration of the silica NCs in tumor tissues. We performed the tumor penetration study by incubating LLC tumors (grown in C57BL/6 mice) for 48 h in culture medium containing equal concentration of IR20, IR50, or IR200. The tumor sections (20 μm in thickness) were then analyzed by NIR fluorescence microscope. As shown in Figure 2c, the size dependency of tumor penetration was obvious with IR20 penetrating tumor tissue with the greatest depth from the periphery of the tumors, followed by IR50 with intermediate penetration depth and IR200 with limited tumor penetration. To quantify the penetration, we defined the tumor tissue penetration depth as the distance from the periphery of the tumor to the site where the fluorescence intensity decreases by 95% as compared to the tumor periphery fluorescent intensity. The penetration depths of IR20, IR50, and IR200 were found to be 1396, 660, and 88 μm, respectively (Figure 2d). The penetration depth of IR20 is 2 and 16 times greater than that of IR50 and IR200, respectively. To verify the silica NC size dependency on tumor penetration *in vivo*, we intravenously administered RITC20, RITC50, and RITC200 to LLC-bearing C57BL/6 mice *via* tail vein. Tumors were collected 24 h post-injection, fixed, and sectioned. After the blood vessel was stained with human Von Willebrand Factor antibody (green, FITC channel in Figure 2e), the tumor tissues were then analyzed using a confocal microscope to study the distribution of NCs in tumor tissues relative to the blood vessels. This study showed the effect of biodistribution and diffusion collectively. RITC20 and RITC50 significantly outperformed RITC200 and diffused away from and situated distally to the blood vessel. Comparing the representative regions of interest, the fluorescence intensity of RITC20 is 4 and 22 times greater than RITC50 and RITC200, respectively. This observation of size-dependent *in vivo* penetration is consistent with the observations from the tumor penetration studies using an *ex vivo* model (Figure 2c) and the size-dependent biodistribution studies (Figure 2b).

While the NCs diffuse into tumor tissue, whether the NCs stay in the interstitial extracellular matrix or are

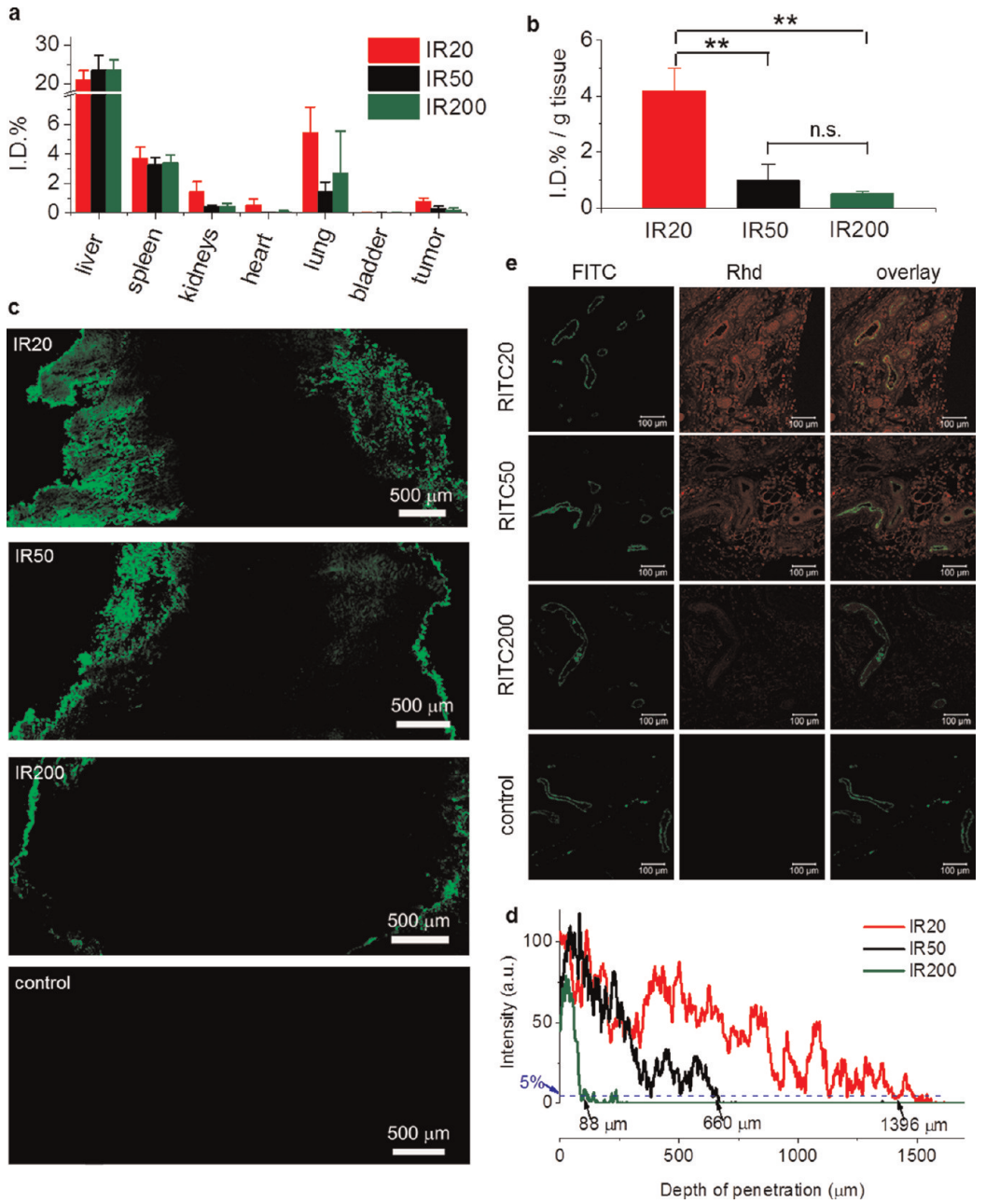

Figure 2. Size effect on biodistribution and tumor penetration. (a,b) C57BL/6 mice bearing Lewis lung carcinoma (LLC) ($n = 3$) were injected intravenously with IR20, IR50, and IR200. Mice were euthanized, and the tissues were collected, excised to 2 mm or less in thickness, and analyzed ($\lambda_{emission} = 800$ nm) on an Odyssey infrared imaging system. The fidelity of utilizing Odyssey infrared imaging system for quantitative IR analysis in biological tissues was verified in a series of control studies (Figure S6). All of the organ distribution is presented as percentage of injected dose (ID%, a). Tumor accumulation data are presented as percentage of injected dose per gram of tumor tissue (I.D.%/g tissue, b). Student's *t* test (two-tailed) was performed for statistical analysis: n.s., not significant; highly statistical significant with 99% confidence, $^{**}p < 0.01$. (c,d) LLC tumors ($n = 3$) were *ex vivo* cultured with IR20, IR50, or IR200 in cell culture medium for 48 h. The tumors without any treatment served as the control. The tumor sections of treatment groups (intersections, 20 μm in thickness) were collected by cryostat, mounted on glass slides, and analyzed on a fluorescence microscope ($\lambda_{excitation} = 780$ nm) (c). A tiling image was taken with fixed exposure time to show the NC penetration in tumor sections. Scale bar = 500 μm. The fluorescence profile in the tumor section was analyzed by Image J to show the depth of NC penetration in tumor tissues (d). To quantify the penetration, we defined the tumor tissue penetration depth as the distance from the periphery of the tumor to the site where the fluorescence intensity decreases by 95% as compared to the fluorescent intensity at tumor periphery. The penetration depths of IR20, IR50, and IR200 were found to be 1396, 660, and 88 μm, respectively. (e) C57BL/6 mice bearing LLC tumors ($n = 3$) were injected intravenously with RITC20, RITC50, or RITC200. Mice were euthanized and dissected 24 h post-injection. Tumor sections (intersections, 5 μm in thickness) were collected in paraffin and mounted on glass slides. Fluorescence images were taken on a Zeiss LSM 700 confocal microscope. Representative two-color composite images showing the perivascular distribution of RITC-NCs (red, Rhd channel) relative to the blood vessels (green, FITC channel) in tissue sections of LLC tumors are shown and overlaid. Scale bar = 100 μm.

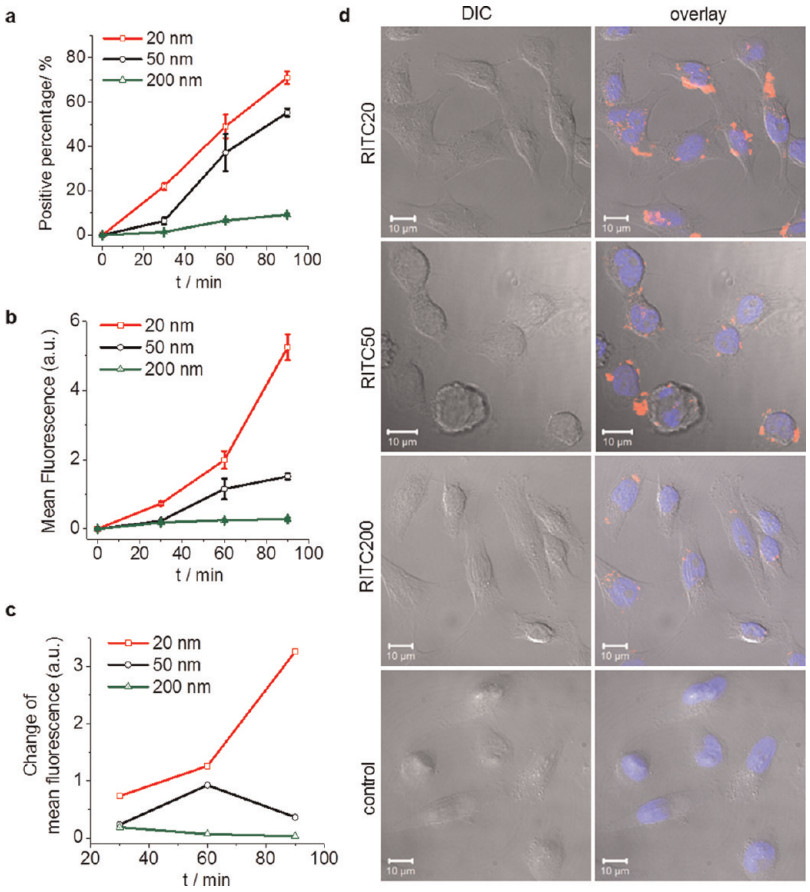

Figure 3. NC size effect on cellular internalization. (a−c) Internalization of RITC-NCs into HeLa cells over 90 min incubation at 37 °C evaluated by the percentage of cells containing internalized NCs (a), mean fluorescence of treated cells (b), and change of mean fluorescence every 30 min (c). (d) Confocal laser scanning microscopy images of HeLa cells after 1 h incubation at 37 °C with RITC20, RITC50, and RITC200 (red). The nuclei of cells were stained by 4′-6-diamidino-2-phenylindole (DAPI) (blue). Left panel: differential interference contrast (DIC). Right panel: overlay of DIC, DAPI, and Rhd channels. Scale bar = 10 μm.

internalized and reside inside the cells should impact the penetration depth in tumor tissue as well as the capability of retention. We thus compared the size-dependent uptake of these NCs in HeLa cells. Cellular internalization of RITC20, RITC50, or RITC200 into the HeLa cells for 30, 60, or 90 min incubation was analyzed by fluorescence-activated flow cytometry (FACS) to assess the kinetics of NC internalization (Figure 3a). We found that smaller NCs were internalized into HeLa cells faster and more efficiently than NCs with larger size, in terms of both percentage of the fluorescent cells and total accumulated mean fluorescence intensity. The number of fluorescent cells accounts for 1.4, 6.6, and 9.2% of the total treated cells for 30, 60, and 90 min incubation with RITC200. These numbers were 6.6, 37.2, and 55.2% for RITC50, and 21.9, 49.1, and 71.0% for RITC20, respectively (Figure 3a). The fluorescence intensities of cells for 30, 60, and 90 min incubation with RITC200 were 0.18, 0.25, and 0.28, in arbitrary units of FACS. These numbers were 0.23, 1.15, and 1.52 for RITC50 and 0.73, 1.99, and 5.25 for RITC20, respectively (Figure 3b). The 20 nm NC was therefore internalized 18.7 and 3.5 times more than 200 and 50 nm NCs for a total of 90 min incubation. Interestingly, comparing the fluorescence intensity change of the three 30 min blocks (0−30, 30−60, and 60−90 min), we found that the rate of internalization of 20 nm NC (RITC20) in HeLa cells was accelerating in the first 90 min while the accumulation of 200 nm NC (RITC200) was evidently deaccelerating (Figure 3c). For RITC200, 90 min incubation *versus* 30 min incubation resulted in an increase of the number of the fluorescent cells by 660% (9.2% *vs* 1.4%), but the total accumulated fluorescence intensity was only increased by 56% (0.28 *vs* 0.18), suggesting that not all internalized RITC200 can be effectively retained inside the cells and exocytosis might occur simultaneously.[33] In contrast, 90 min incubation *versus* 30 min incubation of RITC20 resulted in an increase of the number of fluorescence cells by 340% (71% *vs* 21%) and the total accumulated fluorescence intensity by 720% (5.25 *vs* 0.73), clearly indicating that the 20 nm particle can be effectively internalized and retained in the cells, and the internalization/retention process become more favorable during the course of the study. The size-dependent cell uptake and retention was also verified by confocal microscopy study (Figure 3d), which demonstrated that NCs with smaller sizes were internalized

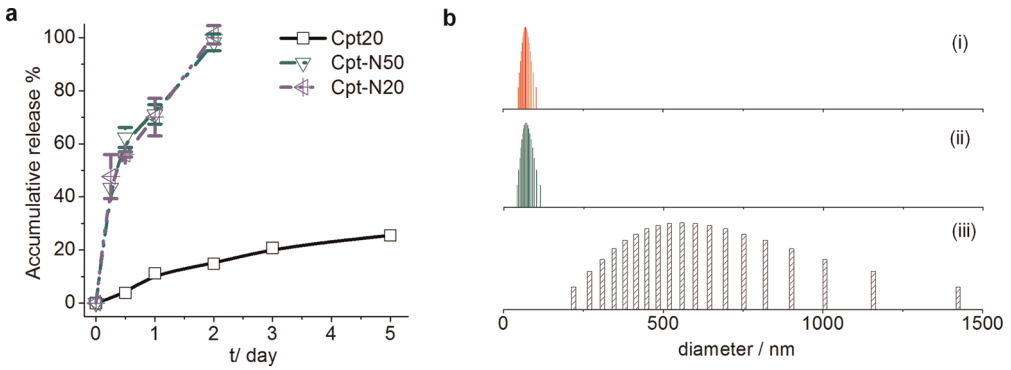

Figure 4. Tunable drug release profiles and solid-form formulation of drug−silica nanoconjugates. (a) Release kinetics of Cpt-NCs with different linkers and sizes in 50% human serum at 37 °C. (b) NC size distributions measured by dynamic light scattering (DLS) before lyophilization (i), after lyophilization in the presence of dextrose (5%) and reconstituted with water (ii), and after lyophilization in the absence of dextrose and reconstituted with water (iii).

and retained inside the cells more efficiently than the NCs with larger sizes.

The 20 nm silica NC outperforms the 50 nm NC and the 200 nm NC by ~2−5 and ~10−20 times, respectively, in terms of biodistribution, tumor tissue penetration, and internalization to cancer cells. Collectively, 20 nm NCs breach the three physiological barriers (systemic, tissue, and cellular) that are critical to drug delivery significantly better than larger particles. We are currently exploring whether the NCs containing a targeting ligand will follow the same size dependency as what we observed in this study with the use of nontargeting NCs. Because particles less than 10 nm may be subject to significant renal clearance and rapid fenestration into other tissues (*e.g.*, lymphatic system), which is undesirable for sustained circulation that is critical to passive targeting and tumor tissue accumulation *via* EPR effect, the NC around 20 nm may be close to the optimal size for drug delivery application.

Silica NCs have other promising properties that are noteworthy. First, this nanofabrication process, as shown in Scheme 1, allows the incorporation of drug (dye) molecules in high yields (up to 24%) (Table 1) that are comparable to or higher than the FDA-approved drug delivery systems, such as Doxil (~10%).[34] Drug burst release is a long-standing formulation challenge of nanocarriers with drug encapsulated in polymeric NPs or adsorbed in mesoporous silica NPs, which causes undesirable dose dumping, significant side effects, and reduced long-term therapeutic efficacy. Since the drug release kinetics of drug-NCs is determined by the hydrolysis of the thioether ester bond linker, the release kinetics of drug from NCs are more controllable with essentially no burst release (Figure 4a). In human serum, Cpt20 with the hydrophobic thioether ester linker between Cpt and the silica particles showed sustained drug release with 14.8% of CPT being released in 48 h (Figure 4a); the IC_{50} value of Cpt20 in HeLa cells was found to be 220 nM. When the linker was changed to a hydrophilic amine ester as in Cpt-N20 (entry 20, Table 1, and Figure 1c), which was prepared by using **7** as the corresponding drug-containing silane reagent (Scheme 1), the Cpt release kinetics can be dramatically accelerated with Cpt being 100% released within 48 h, resulting in a much lower IC_{50} value (9.0 nM, Table S4). This could be due to the fact that hydrophilic amine ester is more assessable by water and esterase, which can accelerate the cleavage of the ester bond. By controlling the feed ratio of **2**/**7** during Cpt-NC fabrication to the ratios of these two different linkers, the Cpt release half-life can potentially be precisely adjusted ranging from 24 h to about 2 weeks.

Besides controlled particle size, drug loading, and release kinetics, other issues critical to the clinical translation of NP drug delivery system, such as scalability, lyophilizability, and toxicity, should also be addressed. These issues may also present the bottleneck to the clinical translation of a nanomedicine. We found the silane chemistry could be easily used for the large-scale

TABLE 2. Lyophilization of Silica NC

entry	lyoprotectant	*m*(Lyo)/*m*(NP)[a]	D_0/nm[b]	*D*/nm[c]	D/D_0[d]	aggr. (Y/N)[e]
1	none	N/A	102.0	233.5	2.29	Y
2	sodium chloride	10	102.0	2295.1	22.50	Y
3	BSA	1	102.0	139.1	1.36	N
4	BSA	5	102.0	120.6	1.18	N
5	BSA	10	102.0	142.0	1.39	N
7	dextrose	1	102.0	108.1	1.06	N
8	dextrose	5	102.0	101.5	1.00	N
9	dextrose	10	102.0	99.5	0.98	N
10	none	N/A	69.8	558.8	8.01	Y
11	sodium chloride	10	69.8	2910.7	41.70	Y
12	BSA	1	69.8	103.6	1.48	N
13	BSA	5	69.8	91.0	1.30	N
14	BSA	10	69.8	97.8	1.40	N
15	dextrose	1	69.8	84.3	1.21	N
16	dextrose	5	69.8	68.9	0.99	N
17	dextrose	10	69.8	71.2	1.02	N

[a] Mass ratio of lyoprotectant (Lyo) to NP. [b] D_0 = NP size determined by DLS before lyophilization. [c] *D* = NP size determined by DLS after lyophilization in the presence of the corresponding lyoprotectant and reconstitution with water. [d] The ratio of NP size after and before lyophilization. [e] Observation of NP aggregation (aggr.) after lyophilization and reconstitution with water (Y = aggregated; N = no aggregation).

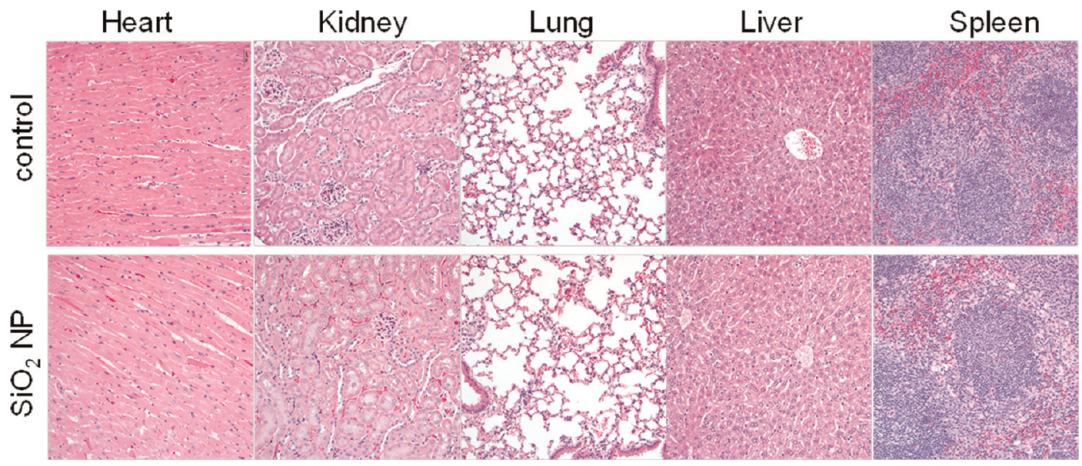

Figure 5. Histopathology of mouse tissues following an intravenous injection of silica nanoparticles *via* tail vein. Representative sections of various organs taken from control mice receiving PBS and mice receiving 250 mg/kg 50 nm blank silica nanoparticles 24 h post-injection were stained by hematoxylin and eosin. No organs of a mouse given silica nanoparticles showed any acute inflammations.

preparation of drug-containing NCs. We tested the preparation of ~1 g of 50 nm Cpt-NC in one pot and successfully obtained NCs with the expected size (46.4 ± 4.6 nm) in quantitative yield within 1 day (entry 22, Table 1, Figure S2). The NP fabrication process that allows preparation of very small drug delivery NPs with remarkable control over size and monodispersity and with excellent scalability is unprecedented and offers clear advantages over many other nanomedicine preparation methods.

Aiming to formulate solid silica NCs without aggregation, we tested the lyophilization of silica NCs in the presence of various lyoprotectants (Table 2). We found dextrose was overall the best lyoprotectant for silica NC. Silica NCs lyophilized in 1 mL of 5% dextrose solution (known as D5W, routinely used for drug administration in clinic) resulted in solid formulation of silica NCs with essentially no change of particle sizes after lyophilization and reconstitution in water (Figure 4b).

Recent studies showed that silica NPs can decompose in blood within a few days,[35,36] suggesting that this class of NPs can be eliminated by either hepatic or renal clearance,[37,38] thereby minimizing concerns for cumulative tissue damage and associated toxicity. *In vitro* study (MTT assay; Table S4) showed almost no toxicity of the blank silica NPs (IC_{50} > 1 mM). Acute *in vivo* toxicity experiments were performed after i.v. administration of the 50 nm silica NPs in C57BL/6 mice at a very high, single dose up to 250 mg/kg. There was no mortality or deterioration under general conditions observed in mice treated with silica NPs. In addition, there were no treatment-related clinical signs or change of body weights. Representative sections of various organs taken 24 h after injections from control mice receiving PBS and mice receiving silica NPs were stained by hematoxylin and eosin and evaluated by an independent pathologist (Figure 5). The absence of immune or inflammatory reactions after NC administration supports their lack of toxicity. To facilitate faster degradation, we prepared bis-silane agents containing pH-sensitive ester (**8**) or orthoester domain (**9**). They can be very successfully incorporated to silica NCs to make monodisperse silica NCs (entries 23−26, Table 1, Figure S7). These results demonstrated that the perfect size control for this silica NC formulation method was independent of the silane reagents used (*e.g.*, in the context of using **8** or **9**, entries 23−26, Table 1) or the linker properties (*e.g.*, in the context of using **7**, entries 20−21, Table 1). Studies of the *in vivo* degradation and clearance of regular silica NCs and **8**- or **9**-containing silica NCs are underway.

CONCLUSIONS

Silica NPs have been used in various drug and gene delivery applications.[22,23,39−60] For example, silica NPs with stably bound photosensitizer were used for photodynamic therapy;[57] mesoporous silica NPs were explored extensively for the encapsulation and delivery of chemotherapeutics;[46,48,49,51−53,58,60−63] silica NPs were also used in gene delivery.[47,48,59,64] These studies set up the cornerstone for the continuous advancement and novel design of silica NP-based nanomedicine. In this paper, we streamlined a process for developing a potentially clinically applicable drug−silica nanoconjugate delivery system with well-controlled physicochemical and pharmacological properties. To the best of our knowledge, this is the only report of a drug/dye delivery nanomedicine platform that can be easily prepared in gram or larger scale in dry powder form and can be controlled and formulated to any desirable size ranging from 20 to 200 nm with monodisperse particle size distribution (CV ≤ 10%). The *in vitro* and *in vivo* studies using NCs with discrete sizes of 20, 50, and 200 nm demonstrate that smaller particle size is more efficient in bypassing the systemic, tissue, and cellular barriers, the three physiological barriers that are critical for effective

drug delivery. Collectively, 20 nm silica NCs outperform 50 and 200 nm NCs by ~2–5 and ~10–20 times, respectively, in terms of tumor accumulation, tumor tissue penetration, and cell internalization. Due to formulation challenges, most of the FDA-approved drug delivery nanomedicines and others under clinical or preclinical investigations have sizes over 100 nm. Our study not only demonstrates substantial opportunities to further reduce nanomedicine size that may favorably impact their *in vitro* and *in vivo* performance, in particular, for sizes ranging from 20 to 50 nm, but also provides a platform technology to make such particles with these desired properties for clinical drug delivery applications and fundamental studies.

METHODS

General Procedure for the Preparation of Pyr–Silica Nanoconjugates[28,65–67]**.** Methanol (1.0 mL), DI water (0.27 mL), and concentrated ammonia (0.24 mL) were mixed. TEOS (62.5 μL, 0.28 mmol) was then added to the solvent mixture followed by the addition of a DMSO solution (20 μL) of **1** (2 mg, 4.3 μmol). The mixture was stirred at a stirring rate of 100 rpm at room temperature for 12 h. The resulting Pyr-NCs were collected by centrifugation at 15k rpm and washed by ethanol (3 × 1 mL). One drop of a dilute solution of silica NCs in ethanol on a silicon wafer was allowed to dry in air and then analyzed by SEM at 5 kV. The NC size (200 nm in this case) was determined by averaging 100 particles on representative SEM image. Fabrication of monodisperse Pyr-NCs with other sizes can be similarly achieved by tuning the concentrations of TEOS, water, and ammonia (Table 1 and Table S1). Cpt-NCs, Ptxl-NCs, RITC-NCs, and IR-NCs with monodisperse, controlled sizes were prepared under similar conditions with the corresponding silane substrates **2**–**7**.

General Procedure for Preparing Cpt- or Ptxl-NCs *via* Modified Stöber Method[45]**.** The silica NCs of various sizes were prepared using the Stöber method as described without the addition of **1**. The obtained silica NCs (4.1 mg) were redispersed in a mixture of EtOH/DI water (0.7 mL/0.2 mL) followed by the addition of **2** (1.7 mg) in DMSO (100 μL). After the mixture was stirred for 10 min, a NaF aqueous solution (10 mg/mL, 25 μL) was added. After 12 h of reaction, **6** (10 mg/mL, 100 μL) was added. The mixture was stirred for another 12 h. The supernatant of the mixture was analyzed by HPLC to determine the unreacted **2** in order to determine the incorporation efficiency of drugs to NCs. The drug loadings were calculated based on the feed ratio of drugs to NCs and the incorporation efficiency. The NCs were collected by centrifugation at 15k rpm. The isolated NCs were washed with ethanol (3 × 1 mL) and redispersed in DI water or 1× PBS buffer before use. The preparation of Ptxl-NC was similar except for addition of **3** (1.0 mg).

Preparation of RITC/IR-NCs *via* Stöber Method. The silica NCs (27.5 mg) of various sizes were prepared as described above without the addition of drug(dye)–sil reagents. After the reaction was complete, without isolating the NCs, a methanol solution of **4** (10 mg/mL, 100 μL) was added to the silica NC solution. The mixture was stirred for 12 h in the dark. A methanol solution of **6** (10 mg/mL, 100 μL) was added. RITC-NCs were collected by centrifugation at 15k rpm, washed with ethanol (3 × 1 mL), and redispersed in DI water or 1× PBS buffer before use. IR-NCs were similarly prepared using **5** instead of **4**.

Preparation of Cpt- or Ptxl-Silica NCs Using Degradable Silane 8 or 9 *via* a Reverse Microemulsion Process. During the NC fabrication through the reverse microemulsion process, Triton X-100 and *n*-hexanol were employed as the surfactant and the cosurfactant, respectively. To prepare 20 nm Cpt-NCs containing a degradable ester bond (Cpt-EB20, Table 1), cyclohexane (7.5 mL), *n*-hexanol (1.8 mL), and Triton X-100 (1.77 mL) were mixed and stirred for 20 min. DI water (480 μL) and **8** (80 μL) were added over the course of 20 min. Ammonia hydroxide (28%, 60 μL) was added to initiate the reaction. After 24 h, **2** (17.9 mg, 0.03 mmol) in dichloromethane solution (500 μL) was added. The reaction solution was stirred for another 12 h. A methanol solution of **6** (10 mg/mL, 600 μL) was added. The supernatant of the mixture was analyzed by HPLC to quantify the unreacted **2** in order to determine the incorporation efficiency of drugs to NCs. The drug loading was determined based on the feed ratio of **2** *versus* **8** and TEOS and the incorporation efficiency of **2** to NC. The emulsion was disrupted by the addition of 10 mL of ethanol. The NC (Cpt-EB20) was collected by centrifugation at 15k rpm and washed with ethanol (3 × 1 mL). Cpt-EB50, Cpt-AB20, and Ptxl-EB20 (entries 23–26, Table 1) were prepared by following similar conditions as summarized in Table 1 and Table S2.

Release Kinetics. The NC (Cpt20, Cpt-N20, or Cpt-N50) was dispersed in 50% reconstituted human serum (Sigma-Aldrich) (0.6 mg NC/mL), equally distributed to 20 vials with 1 mL of NC solution per vial, and then incubated at 37 °C. At selected time intervals, one selected vial of each group was taken out of the incubator. The NC solution was mixed with an equal volume of methanol (1 mL) and centrifuged at 15 000 rpm for 10 min. The supernatant (1 mL) was transferred to an Eppendorf tube without disturbing the precipitates (NCs) and tuned to pH 2 with phosphoric acid (85%, 100 μL). The resulting solution was directly injected into HPLC equipped with an analytical C18 column (Luna C18, 250 × 4.6 mm, 5 μ, Phenomenex, Torrance, CA, USA). A mixture of acetonitrile and water (containing 0.1% TFA) at a volume ratio of 1:3 was used as the mobile phase. The flow rate was set at 1 mL/min. The area of the HPLC peak of the released Cpt (λ_{abs} = 370 nm) was intergraded for the quantification of Cpt as compared to a standard curve of free Cpt prepared separately. The Cpt release kinetic profiles from Cpt20, Cpt-N20, and Cpt-N50 are shown in Figure 4a.

Lyophilization of Silica NPs in the Presence of Lyoprotectants. Silica NPs were prepared at a TEOS/**6** ratio (w/w) of 19.6:1 using Stöber method as described previously (St-B and St-E) and analyzed with DLS. One of the selected lyoprotectants (Table S2) was added at different lyoprotectant/NP ratio (varying from 1:1 to 10:1 w/w) to the NP solution. The solution was lyophilized. The solid-form silica NP/lyoprotectant was reconstituted with 2 mL of DI water to prepare a NP aqueous solution at a concentration of 10 mg/mL. The reconstituted silica NP was analyzed by DLS (Figure 4b). The silica NP lyophilized in the absence of lyoprotectant and reconstituted with water was used as the negative control.

Cellular Internalization of RITC-NCs. The HeLa cells were used to investigate the uptake of RITC20, RITC50, and RITC200 (Table 1). HeLa cells (50 000) were seeded in a 4-well chamber slide for 24 h (37 °C, 5% CO_2). Cells were washed once with opti-MEM and then incubated for 1 h (37 °C, 5% CO_2) with opti-MEM (1 mL) containing 100 μg/mL corresponding RITC-NCs. The cells were then washed by PBS (1 mL) three times, fixed with 4% paraformaldehyde, and subsequently imaged on a confocal laser scanning microscope. Nuclei were stained by DAPI. Cells without the addition of RITC-NCs were imaged as the control. The cell uptake kinetics of RITC-NCs was also studied. HeLa cells (100 000) were seeded in a 12-well plate for 24 h. RITC-NCs (100 μg/mL) were incubated with the cells in opti-MEM (1 mL) over a time course ranging from 30 to 90 min (37 °C, 5% CO_2). The cells were then washed with PBS (3 × 1 mL) and detached *via* trypsinization. Cells were fixed with 4% paraformaldehyde for flow cytometry analysis (10 000 cells analyzed, red fluorescence, PE channel). Both the percentage of the fluorescent cells relative to the total analyzed cells and the fluorescence intensity of the fluorescence-positive cells were assessed. All experiments were performed in triplicate.

***Ex Vivo* Tumor Penetration Study.** C57BL/6 mice (female, 12–13 weeks old) bearing LLC tumors were sacrificed to collect the tumors when the tumors grew to ~7.0–8.0 mm. Tumors (n = 3)

were *ex vivo* cultured with IR20, IR50, or IR200 (Table 1) at a concentration of 3 mg/mL NC in cell medium for 48 h. Tumor without any treatment served as the control. Tumor sections (20 μm thickness) were collected by cryostat and mounted on glass slides. Fluorescent images were taken on a Zeiss Axiovert 200M fluorescence microscope with 780 nm laser excitation. A tiling image was taken with fixed exposure time to show the NC penetration in tumor sections. The fluorescence intensity in tumor sections was analyzed by Image J. To quantify the penetration of NCs, we defined the tumor tissue penetration depth as the distance from the periphery of the tumor to the site where the fluorescence intensity decreased by 95% as compared to the fluorescent intensity at the tumor periphery.

***In Vivo* Tumor Penetration Study.** LLC tumor-bearing C57BL/6 mice were divided randomly into groups of three (n = 3) and were treated when the mean tumor diameter was in the range of ~5.0−6.0 mm. Each animal received a PBS solution of RITC20, RITC50, or RITC200 (200 μL, 50 mg/mL) through tail vein administration. The animals were euthanized 24 h after administration. The tumors were collected, fixed by 10% formalin, and then embedded in paraffin prior for tissue sectioning and immunohistochemical staining. A tissue section with approximate thickness of 5 μm was collected from each tumor, mounted on glass slides, and allowed to air-dry. Fluorescence images were taken on a Zeiss LSM 700 confocal microscope. Tissue sections were imaged with a 10×/0.3 lens. Developing tumor neovasculature within each tumor section was identified by the expression of Von Willebrand Factor (Factor VIII-related antigen) by incubating slides with a rabbit polyclonal anti-human Factor VIII antibody (1:200) for 30 min at room temperature. Following primary antibody incubation, glass slides were stained with a FITC-conjugated goat polyclonal anti-rabbit antibody (1/250) for 4 h in the dark, then coverslipped using VECTASHIELD mounting media (Burlingame, CA). FITC fluorescence representing endothelial cells was visualized using 488 nm laser excitation. Red fluorescence of rhodamine, representing silica NCs, was visualized with 555 nm laser excitation.

***In Vivo* Biodistribution Study.** C57BL/6 mice bearing LLC tumors (~5.0−6.0 mm) (n = 3) were divided into three groups, minimizing tumor size variations between groups. Mice were injected intravenously with IR20, IR50, and IR200 at a dose of 150 mg/kg. Mice were euthanized and dissected 24 h post-injection. The major organs (liver, spleen, kidney, heart, bladder, lung, and tumor) were collected and fixed in 10% formalin. The fluorescent intensity of IR-NCs in each organ was measured *ex vivo* at 800 nm emission using Odyssey infrared mouse imaging system. The concentration of the IR-NCs in each organ was determined by comparing its fluorescent intensity against a standard curve of IR-NCs (Figure S6).

***In Vivo* Biocompatibility Study.** Silica NCs of 50 nm in diameter were prepared by St-C using TEOS/**6** = 19.6/1. They were administered intravenously (200 μL, 25 mg/mL) *via* lateral tail vein to the C57BL/6 mice (n = 3) at a dose of 250 mg of silica NC/kg. The animals were sacrificed 24 h later by carbon dioxide. Organs including heart, lung, liver, spleen, and kidney were fixed in 10% neutral buffered formalin for 48 h. The fixed tissues were then processed and trimmed, embedded in paraffin, sectioned to a thickness of 5 μm, and stained with hematoxylin and eosin for microscopic examination. Characterization of all the collected target tissues for inflammatory cell infiltrate including macrophages and neutrophils was performed by systemic microscopic evaluation at 400× magnification and analyzed by an independent pathologist.

Statistical Analyses. Student's t-test (two tailed) comparisons at 95% confidence interval were used for statistical analysis. The results were deemed significant at $0.01 < p \leq 0.05$, highly significant at $0.001 < p \leq 0.01$, and extremely significant at $p \leq 0.001$.

Conflict of Interest: The authors declare no competing financial interest.

Acknowledgment. J.C. acknowledges supports from the NIH (Director's New Innovator Award program 1DP2OD007246-01 and 1R21CA152627). L.T. was funded at University of Illinois at Urbana—Champaign from NIH National Cancer Institute Alliance for Nanotechnology in Cancer `Midwest Cancer Nanotechnology Training Center' Grant R25 CA154015A.

Supporting Information Available: Synthesis and characterization of silane reagents. SEM images, calibration, formulation condition, and toxicity of silica particles. This material is available free of charge *via* the Internet at http://pubs.acs.org.

Note Added after ASAP Publication. This paper was published online April 24, 2012. Corrections were made to Table 1, Scheme 1, and Figure 5, and the corrected version was reposted May 2, 2012.

REFERENCES AND NOTES

1. Duncan, R. Polymer Conjugates as Anticancer Nanomedicines. *Nat. Rev. Cancer* **2006**, *6*, 688–701.
2. Davis, M. E.; Chen, Z.; Shin, D. M. Nanoparticle Therapeutics: An Emerging Treatment Modality for Cancer. *Nat. Rev. Drug Discovery* **2008**, *7*, 771–782.
3. Ferrari, M. Cancer Nanotechnology: Opportunities and Challenges. *Nat. Rev. Cancer* **2005**, *5*, 161–171.
4. Pornpattananangkul, D.; Zhang, L.; Olson, S.; Aryal, S.; Obonyo, M.; Vecchio, K.; Huang, C. M.; Zhang, L. F. Bacterial Toxin-Triggered Drug Release from Gold Nanoparticle-Stabilized Liposomes for the Treatment of Bacterial Infection. *J. Am. Chem. Soc.* **2011**, *133*, 4132–4139.
5. Shim, M. S.; Kwon, Y. J. Acid-Transforming Polypeptide Micelles for Targeted Nonviral Gene Delivery. *Biomaterials* **2010**, *31*, 3404–3413.
6. Bae, J. W.; Pearson, R. M.; Patra, N.; Sunoqrot, S.; Vukovic, L.; Kral, P.; Hong, S. Dendron-Mediated Self-Assembly of Highly PEGylated Block Copolymers: A Modular Nanocarrier Platform. *Chem. Commun.* **2011**, *47*, 10302–10304.
7. Medina, S. H.; Tekumalla, V.; Chevliakov, M. V.; Shewach, D. S.; Ensminger, W. D.; El-Sayed, M. E. H. *N*-Acetylgalactosamine-Functionalized Dendrimers as Hepatic Cancer Cell-Targeted Carriers. *Biomaterials* **2011**, *32*, 4118–4129.
8. Bagalkot, V.; Farokhzad, O. C.; Langer, R.; Jon, S. An Aptamer-Doxorubicin Physical Conjugate as a Novel Targeted Drug-Delivery Platform. *Angew. Chem., Int. Ed.* **2006**, *45*, 8149–8152.
9. Ghadiali, J. E.; Lowe, S. B.; Stevens, M. M. Quantum-Dot-Based FRET Detection of Histone Acetyltransferase Activity. *Angew. Chem., Int. Ed.* **2011**, *50*, 3417–3420.
10. Wagner, V.; Dullaart, A.; Bock, A. K.; Zweck, A. The Emerging Nanomedicine Landscape. *Nat. Biotechnol.* **2006**, *24*, 1211–1217.
11. Stewart, S.; Jablonowski, H.; Goebel, F.; Arasteh, K.; Spittle, M.; Rios, A.; Aboulafia, D.; Galleshaw, J.; Dezube, B. Randomized Comparative Trial of PEGylated Liposomal Doxorubicin *versus* Bleomycin and Vincristine in the Treatment of AIDS-Related Kaposi's Sarcoma. International PEGylated Liposomal Doxorubicin Study Group. *J. Clin. Oncol.* **1998**, *16*, 683–691.
12. Dreher, M. R.; Liu, W. G.; Michelich, C. R.; Dewhirst, M. W.; Yuan, F.; Chilkoti, A. Tumor Vascular Permeability, Accumulation, and Penetration of Macromolecular Drug Carriers. *J. Natl. Cancer Inst.* **2006**, *98*, 335–344.
13. Reddy, S. T.; van der Vlies, A. J.; Simeoni, E.; Angeli, V.; Randolph, G. J.; O'Neil, C. P.; Lee, L. K.; Swartz, M. A.; Hubbell, J. A. Exploiting Lymphatic Transport and Complement Activation in Nanoparticle Vaccines. *Nat. Biotechnol.* **2007**, *25*, 1159–1164.
14. Gratton, S. E. A.; Ropp, P. A.; Pohlhaus, P. D.; Luft, J. C.; Madden, V. J.; Napier, M. E.; DeSimone, J. M. The Effect of Particle Design on Cellular Internalization Pathways. *Proc. Natl. Acad. Sci. U.S.A.* **2008**, *105*, 11613–11618.
15. Jiang, W.; Kim, B. Y. S.; Rutka, J. T.; Chan, W. C. W. Nanoparticle-Mediated Cellular Response Is Size-Dependent. *Nat. Nanotechnol.* **2008**, *3*, 145–150.
16. Mitragotri, S.; Lahann, J. Physical Approaches to Biomaterial Design. *Nat. Mater.* **2009**, *8*, 15–23.
17. Nel, A. E.; Madler, L.; Velegol, D.; Xia, T.; Hoek, E. M. V.; Somasundaran, P.; Klaessig, F.; Castranova, V.; Thompson, M. Understanding Biophysicochemical Interactions at the Nano-Bio Interface. *Nat. Mater.* **2009**, *8*, 543–557.

18. Kim, B.; Han, G.; Toley, B. J.; Kim, C. K.; Rotello, V. M.; Forbes, N. S. Tuning Payload Delivery in Tumour Cylindroids Using Gold Nanoparticles. *Nat. Nanotechnol.* **2010**, *5*, 465–472.
19. Jin, Y.; Gao, X. Plasmonic Fluorescent Quantum Dots. *Nat. Nanotechnol.* **2009**, *4*, 571–576.
20. Farokhzad, O. C.; Cheng, J. J.; Teply, B. A.; Sherifi, I.; Jon, S.; Kantoff, P. W.; Richie, J. P.; Langer, R. Targeted Nanoparticle–Aptamer Bioconjugates for Cancer Chemotherapy *in Vivo*. *Proc. Natl. Acad. Sci. U.S.A.* **2006**, *103*, 6315–6320.
21. Smith, A. M.; Mohs, A. M.; Nie, S. Tuning the Optical and Electronic Properties of Colloidal Nanocrystals by Lattice Strain. *Nat. Nanotechnol.* **2009**, *4*, 56–63.
22. Decuzzi, P.; Godin, B.; Tanaka, T.; Lee, S. Y.; Chiappini, C.; Liu, X.; Ferrari, M. Size and Shape Effects in the Biodistribution of Intravascularly Injected Particles. *J. Controlled Release* **2010**, *141*, 320–327.
23. Yu, T.; Malugin, A.; Ghandehari, H. Impact of Silica Nanoparticle Design on Cellular Toxicity and Hemolytic Activity. *ACS Nano* **2011**, *5*, 5717–5728.
24. Wang, H.; Wang, S. T.; Su, H.; Chen, K. J.; Armijo, A. L.; Lin, W. Y.; Wang, Y. J.; Sun, J.; Kamei, K.; Czernin, J.; *et al.* A Supramolecular Approach for Preparation of Size-Controlled Nanoparticles. *Angew. Chem., Int. Ed.* **2009**, *48*, 4344–4348.
25. Perrault, S. D.; Walkey, C.; Jennings, T.; Fischer, H. C.; Chan, W. C. W. Mediating Tumor Targeting Efficiency of Nanoparticles through Design. *Nano Lett.* **2009**, *9*, 1909–1915.
26. Goodman, T. T.; Olive, P. L.; Pun, S. H. Increased Nanoparticle Penetration in Collagenase-Treated Multicellular Spheroids. *Int. J. Nanomed.* **2007**, *2*, 265–274.
27. Cabral, H.; Matsumoto, Y.; Mizuno, K.; Chen, Q.; Murakami, M.; Kimura, M.; Terada, Y.; Kano, M. R.; Miyazono, K.; Uesaka, M.; *et al.* Accumulation of Sub-100 nm Polymeric Micelles in Poorly Permeable Tumours Depends on Size. *Nat. Nanotechnol.* **2011**, *6*, 815–823.
28. Stober, W.; Fink, A.; Bohn, E. Controlled Growth of Monodisperse Silica Spheres in Micron Size Range. *J. Colloid Interface Sci.* **1968**, *26*, 62–69.
29. Stein, A.; Melde, B. J.; Schroden, R. C. Hybrid Inorganic–Organic Mesoporous Silicates—Nanoscopic Reactors Coming of Age. *Adv. Mater.* **2000**, *12*, 1403–1419.
30. Sun, S. H.; Zeng, H.; Robinson, D. B.; Raoux, S.; Rice, P. M.; Wang, S. X.; Li, G. X. Monodisperse MFe_2O_4 (M = Fe, Co, Mn) Nanoparticles. *J. Am. Chem. Soc.* **2004**, *126*, 273–279.
31. Caliceti, P.; Veronese, F. M. Pharmacokinetic and Biodistribution Properties of Poly(ethylene glycol)-Protein Conjugates. *Adv. Drug Delivery Rev.* **2003**, *55*, 1261–1277.
32. Maeda, H.; Wu, J.; Sawa, T.; Matsumura, Y.; Hori, K. Tumor Vascular Permeability and the EPR Effect in Macromolecular Therapeutics: A Review. *J. Controlled Release* **2000**, *65*, 271–284.
33. Chithrani, B. D.; Chan, W. C. W. Elucidating the Mechanism of Cellular Uptake and Removal of Protein-Coated Gold Nanoparticles of Different Sizes and Shapes. *Nano Lett.* **2007**, *7*, 1542–1550.
34. O'Brien, M. E. R.; Wigler, N.; Inbar, M.; Rosso, R.; Grischke, E.; Santoro, A.; Catane, R.; Kieback, D. G.; Tomczak, P.; Ackland, S. P.; *et al.* Reduced Cardiotoxicity and Comparable Efficacy in a Phase III Trial of PEGylated Liposomal Doxorubicin Hcl (Caelyx/Doxil®) *versus* Conventional Doxorubicin for First-Line Treatment of Metastatic Breast Cancer. *Ann. Oncol.* **2004**, *15*, 440–449.
35. Finnie, K. S.; Waller, D. J.; Perret, F. L.; Krause-Heuer, A. M.; Lin, H. Q.; Hanna, J. V.; Barbe, C. J. Biodegradability of Sol–Gel Silica Microparticles for Drug Delivery. *J. Sol–Gel Sci. Technol.* **2009**, *49*, 12–18.
36. Park, J. H.; Gu, L.; von Maltzahn, G.; Ruoslahti, E.; Bhatia, S. N.; Sailor, M. J. Biodegradable Luminescent Porous Silicon Nanoparticles for *In Vivo* Applications. *Nat. Mater.* **2009**, *8*, 331–336.
37. Cho, M. J.; Cho, W. S.; Choi, M.; Kim, S. J.; Han, B. S.; Kim, S. H.; Kim, H. O.; Sheen, Y. Y.; Jeong, J. Y. The Impact of Size on Tissue Distribution and Elimination by Single Intravenous Injection of Silica Nanoparticles. *Toxicol. Lett.* **2009**, *189*, 177–183.
38. He, X. X.; Nie, H. L.; Wang, K. M.; Tan, W. H.; Wu, X.; Zhang, P. F. *In Vivo* Study of Biodistribution and Urinary Excretion of Surface-Modified Silica Nanoparticles. *Anal. Chem.* **2008**, *80*, 9597–9603.
39. Li, L. L.; Tang, F. Q.; Liu, H. Y.; Liu, T. L.; Hao, N. J.; Chen, D.; Teng, X.; He, J. Q. *In Vivo* Delivery of Silica Nanorattle Encapsulated Docetaxel for Liver Cancer Therapy with Low Toxicity and High Efficacy. *ACS Nano* **2010**, *4*, 6874–6882.
40. Della Rocca, J.; Huxford, R. C.; Comstock-Duggan, E.; Lin, W. Polysilsesquioxane Nanoparticles for Targeted Platin-Based Cancer Chemotherapy by Triggered Release. *Angew. Chem., Int. Ed.* **2011**, *50*, 10330–10334.
41. Unger, K.; Rupprecht, H.; Valentin, B.; Kircher, W. The Use of Porous and Surface Modified Silicas as Drug Delivery and Stabilizing Agents. *Drug Dev. Ind. Pharm.* **1983**, *9*, 69–91.
42. Wang, L.; Wang, K. M.; Santra, S.; Zhao, X. J.; Hilliard, L. R.; Smith, J. E.; Wu, J. R.; Tan, W. H. Watching Silica Nanoparticles Glow in the Biological World. *Anal. Chem.* **2006**, *78*, 646–654.
43. Benezra, M.; Penate-Medina, O.; Zanzonico, P. B.; Schaer, D.; Ow, H.; Burns, A.; DeStanchina, E.; Longo, V.; Herz, E.; Iyer, S.; *et al.* Multimodal Silica Nanoparticles Are Effective Cancer-Targeted Probes in a Model of Human Melanoma. *J. Clin. Invest.* **2011**, *121*, 2768–2780.
44. Yan, E. Y.; Fu, Y. L.; Wang, X.; Ding, Y.; Qian, H. Q.; Wang, C. H.; Hu, Y.; Jiang, X. Q. Hollow Chitosan-Silica Nanospheres for Doxorubicin Delivery to Cancer Cells with Enhanced Antitumor Effect *in Vivo*. *J. Mater. Chem.* **2011**, *21*, 3147–3155.
45. Jin, Y. H.; Lohstreter, S.; Pierce, D. T.; Parisien, J.; Wu, M.; Hall, C.; Zhao, J. X. J. Silica Nanoparticles with Continuously Tunable Sizes: Synthesis and Size Effects on Cellular Contrast Imaging. *Chem. Mater.* **2008**, *20*, 4411–4419.
46. Klichko, Y.; Liong, M.; Choi, E.; Angelos, S.; Nel, A. E.; Stoddart, J. F.; Tamanoi, F.; Zink, J. I. Mesostructured Silica for Optical Functionality, Nanomachines, and Drug Delivery. *J. Am. Ceram. Soc.* **2009**, *92*, S2–S10.
47. Xia, T. A.; Kovochich, M.; Liong, M.; Meng, H.; Kabehie, S.; George, S.; Zink, J. I.; Nel, A. E. Polyethyleneimine Coating Enhances the Cellular Uptake of Mesoporous Silica Nanoparticles and Allows Safe Delivery of SiRNA and DNA Constructs. *ACS Nano* **2009**, *3*, 3273–3286.
48. Meng, H. A.; Liong, M.; Xia, T. A.; Li, Z. X.; Ji, Z. X.; Zink, J. I.; Nel, A. E. Engineered Design of Mesoporous Silica Nanoparticles To Deliver Doxorubicin and P-Glycoprotein SiRNA To Overcome Drug Resistance in a Cancer Cell Line. *ACS Nano* **2010**, *4*, 4539–4550.
49. Meng, H.; Yang, S.; Li, Z. X.; Xia, T.; Chen, J.; Ji, Z. X.; Zhang, H. Y.; Wang, X.; Lin, S. J.; Huang, C.; *et al.* Aspect Ratio Determines the Quantity of Mesoporous Silica Nanoparticle Uptake by a Small GTPase-Dependent Macropinocytosis Mechanism. *ACS Nano* **2011**, *5*, 4434–4447.
50. Burns, A. A.; Vider, J.; Ow, H.; Herz, E.; Penate-Medina, O.; Baumgart, M.; Larson, S. M.; Wiesner, U.; Bradbury, M. Fluorescent Silica Nanoparticles with Efficient Urinary Excretion for Nanomedicine. *Nano Lett.* **2009**, *9*, 442–448.
51. Lai, C. Y.; Trewyn, B. G.; Jeftinija, D. M.; Jeftinija, K.; Xu, S.; Jeftinija, S.; Lin, V. S. Y. A Mesoporous Silica Nanosphere-Based Carrier System with Chemically Removable CdS Nanoparticle Caps for Stimuli-Responsive Controlled Release of Neurotransmitters and Drug Molecules. *J. Am. Chem. Soc.* **2003**, *125*, 4451–4459.
52. Giri, S.; Trewyn, B. G.; Stellmaker, M. P.; Lin, V. S. Y. Stimuli-Responsive Controlled-Release Delivery System Based on Mesoporous Silica Nanorods Capped with Magnetic Nanoparticles. *Angew. Chem., Int. Ed.* **2005**, *44*, 5038–5044.
53. Taylor, K. M. L.; Kim, J. S.; Rieter, W. J.; An, H.; Lin, W. L.; Lin, W. B. Mesoporous Silica Nanospheres as Highly Efficient MRI Contrast Agents. *J. Am. Chem. Soc.* **2008**, *130*, 2154–2155.
54. Rieter, W. J.; Kim, J. S.; Taylor, K. M. L.; An, H. Y.; Lin, W. L.; Tarrant, T.; Lin, W. B. Hybrid Silica Nanoparticles for Multimodal Imaging. *Angew. Chem., Int. Ed.* **2007**, *46*, 3680–3682.

55. Kim, J. S.; Rieter, W. J.; Taylor, K. M. L.; An, H.; Lin, W. L.; Lin, W. B. Self-Assembled Hybrid Nanoparticles for Cancer-Specific Multimodal Imaging. *J. Am. Chem. Soc.* **2007**, *129*, 8962–8963.
56. Barbe, C.; Bartlett, J.; Kong, L. G.; Finnie, K.; Lin, H. Q.; Larkin, M.; Calleja, S.; Bush, A.; Calleja, G. Silica Particles: A Novel Drug-Delivery System. *Adv. Mater.* **2004**, *16*, 1959–1966.
57. Hulchanskyy, T. Y.; Roy, I.; Goswami, L. N.; Chen, Y.; Bergey, E. J.; Pandey, R. K.; Oseroff, A. R.; Prasad, P. N. Organically Modified Silica Nanoparticles with Covalently Incorporated Photosensitizer for Photodynamic Therapy of Cancer. *Nano Lett.* **2007**, *7*, 2835–2842.
58. Torney, F.; Trewyn, B. G.; Lin, V. S. Y.; Wang, K. Mesoporous Silica Nanoparticles Deliver DNA and Chemicals into Plants. *Nat. Nanotechnol.* **2007**, *2*, 295–300.
59. Bharali, D. J.; Klejbor, I.; Stachowiak, E. K.; Dutta, P.; Roy, I.; Kaur, N.; Bergey, E. J.; Prasad, P. N.; Stachowiak, M. K. Organically Modified Silica Nanoparticles: A Nonviral Vector for *In Vivo* Gene Delivery and Expression in the Brain. *Proc. Natl. Acad. Sci. U.S.A.* **2005**, *102*, 11539–11544.
60. Lu, J.; Liong, M.; Zink, J. I.; Tamanoi, F. Mesoporous Silica Nanoparticles as a Delivery System for Hydrophobic Anticancer Drugs. *Small* **2007**, *3*, 1341–1346.
61. Liong, M.; Angelos, S.; Choi, E.; Patel, K.; Stoddart, J. F.; Zink, J. I. Mesostructured Multifunctional Nanoparticles for Imaging and Drug Delivery. *J. Mater. Chem.* **2009**, *19*, 6251–6257.
62. Lu, J.; Liong, M.; Li, Z. X.; Zink, J. I.; Tamanoi, F. Biocompatibility, Biodistribution, and Drug-Delivery Efficiency of Mesoporous Silica Nanoparticles for Cancer Therapy in Animals. *Small* **2010**, *6*, 1794–1805.
63. Ferris, D. P.; Lu, J.; Gothard, C.; Yanes, R.; Thomas, C. R.; Olsen, J. C.; Stoddart, J. F.; Tamanoi, F.; Zink, J. I. Synthesis of Biomolecule-Modified Mesoporous Silica Nanoparticles for Targeted Hydrophobic Drug Delivery to Cancer Cells. *Small* **2011**, *7*, 1816–1826.
64. Hom, C.; Lu, J.; Liong, M.; Luo, H. Z.; Li, Z. X.; Zink, J. I.; Tamanoi, F. Mesoporous Silica Nanoparticles Facilitate Delivery of SiRNA To Shutdown Signaling Pathways in Mammalian Cells. *Small* **2010**, *6*, 1185–1190.
65. Corma, A.; Diaz, U.; Arrrica, M.; Fernandez, E.; Ortega, I. Organic−Inorganic Nanospheres with Responsive Molecular Gates for Drug Storage and Release. *Angew. Chem., Int. Ed.* **2009**, *48*, 6247–6250.
66. Kim, J. W.; Kim, L. U.; Kim, C. K. Size Control of Silica Nanoparticles and Their Surface Treatment for Fabrication of Dental Nanocomposites. *Biomacromolecules* **2007**, *8*, 215–222.
67. Ha, S. W.; Camalier, C. E.; Beck, G. R.; Lee, J. K. New Method To Prepare Very Stable and Biocompatible Fluorescent Silica Nanoparticles. *Chem. Commun.* **2009**, 2881–2883.